

Low Density Interconnected Nanowire Networks

Edward C. Burks,¹ Dustin A. Gilbert,^{1,2} Chad Flores,¹ Thomas E. Felter,³

Supakit Charnvanichborikarn,⁴ Sergei Kucheyev,⁴ Jeffrey Colvin,⁴ and Kai Liu^{1,5,*}

¹*Physics Department, University of California, Davis, CA 95618*

²*Department of Materials Science and Engineering, University of Tennessee, Knoxville, Tennessee
37996, USA*

³*Sandia National Laboratory, Livermore, CA 94551*

⁴*Lawrence Livermore National Laboratory, Livermore, CA 94551*

⁵*Physics department, Georgetown University, Washington, DC 20057*

Abstract

Ion track-etched membranes were used as a template for electrodeposition to realize low density interconnected copper and cobalt nanowire networks. Polycarbonate membranes were first irradiated with energetic Xe⁶⁺ ions at normal incidence and multiple 45° azimuthal angles. The latent tracks were etched to create intersecting nanopores in the polycarbonate matrix. After a thin metallic layer was sputtered onto one side of the now-porous membrane, copper and cobalt were electrodeposited into the pores, filling the membrane with an interconnected wire network. Low density structures were formed from interconnected copper wires produced in this way by folding the wire-filled polycarbonate onto itself several times and dissolving the plastic leaving a freestanding structure with density as low as 40 mg/cm³. Additionally the magnetic reversal properties of cobalt nanowire networks were compared to non-intersecting wires (whose reversal is dominated by wire-to-wire dipole-field demagnetizing interactions) revealing that the presence

of wire intersections changes the magnetic reversal behavior of the nanowires by allowing in-plane domain propagation.

Introduction

As micro- and nanoscale technologies have advanced in the last few decades, so too has the demand for synthesis techniques capable of creating ever smaller and more specialized devices with higher aspect ratios[1]. Key among these nanostructured materials are nanowires, which can have aspect ratios of 1000:1. While single nanowires can have applications in extremely sensitive sensors, weaving many wires together to form a nanowire foam offers additional functionalities unique among nanostructured materials. Nanowire foams, including carbon and silica aerogels for example, have shown promise for applications due to their low density, large specific surface areas, and high porosity; metallic foams possess similar functionality and also high thermal and electrical conductivity[2,3] and chemically reactive surface states. These properties allow for a myriad of applications spanning from structural engineering to medicine, including specific uses as catalysts[4], filters[5], supercapacitors [6] and fuel cells[7].

Nanostructured magnetic materials have been demonstrated as powerful components in a number of technologies, including current and next-generation computing, biomedical applications and advanced motors and generators. Controlling and designing magnetic materials on the nanoscale augments the magnetic energy landscape, resulting in changes in the magnetic behavior. Magnetic nanowire foams will have some of the desirable properties of nanowires, including high shape anisotropy and effectively one-dimensional domain propagation, combined with the benefits of the nanowire foams. However, key challenges exist in forming magnetic

nanowire networks, namely the long-range dipole interactions facilitate agglomeration of the wires. Furthermore, the nanowires in these foams are only weakly connected at their contact point and will likely behave as isolated elements. Fabricating the foam as an interconnected network would allow limited inter-wire domain propagation, and improve electrical and thermal properties.

To realize these unique, interconnected nanowire foams, track-etched polycarbonate membranes were used as a template for electrodeposition of cobalt and copper. The creation of damaged tracks by ion irradiation has been used since the 1960's as a radiation detection method in various solids[8,9]. These damaged tracks can be preferentially etched by chemical means, leaving pores in the irradiated solid[10]. This process is currently used to realize track-etched membranes commercially available today,[11] with applications primarily for nanoporous filters. Another popular, albeit specialized, application of track-etched membranes is for templated fabrication of nanowires by electrodeposition[12]. Due to their application as filters, track-etched membranes are typically irradiated at only a single angle, creating an array of parallel pores in the polycarbonate. By irradiating thin polycarbonate films at multiple angles, the tracks are made to randomly cross, forming an interconnected network. Electrodepositing into this porous structure we are able to realize a new, highly interconnected, nanowire foam structure.

Template production

Circular polycarbonate disks with thicknesses of 3 μm and 6 μm were first irradiated with 19.6 MeV Xe^{6+} ions at normal incidence, then rotated by 45° relative to the disk's normal (along the elevation angle) then rotated at 90° or 180° angles along the azimuthal directions (**Fig. 1a**). The total ion irradiation density was varied from 5×10^7 ions/ cm^2 to 4×10^9 ions/ cm^2 . The energetic particles penetrate through the entire thickness of the membranes and create latent damaged tracks (**Fig. 1b**). Next, each side of the membrane is exposed to an ultraviolet (UV) ozone cleaning system

for 3 minutes. This step further breaks the crosslinking in the damaged areas, making these regions more susceptible to chemical etching.[13] The tracks were then etched with intermittent sonication in 6 M NaOH at room temperature. As a result of the UV irradiation, the pores etch quickly along the damage path and slowly along the direction away from the track, thus forming cylindrical pores. After etching the damaged regions, the resultant voids form an intersecting nanopore network (**Fig. 1c**). For a given etchant, the etching time then directly controls the pore diameter. In this work nanoporous templates were created with pore diameters ranging from 75 nm to 350 nm.

Synthesis of interconnected nanowire networks

The interconnected nanowire foam was fabricated by using electrodeposition to fill the pore network. As a first step, a 500 nm nonmagnetic Cu layer was deposited onto one side of the membrane by DC magnetron sputtering to seal the pores in the membrane, and also serve as the working electrode (**Fig. 1d**). Electrodeposition of Cu and Co nanowires was performed with an electrolyte containing 40 g/L copper sulfate or cobalt sulfate, respectively, and 40 g/L boric acid.[14-16] A platinum counter electrode and a Ag^+/AgCl reference electrode are used. Deposition current was monitored until a sudden increase in current was observed, indicating that the pores were filled and that overdeposition was beginning, at which point the potential was removed and the membrane taken out of the cell (**Fig. 1e**). In order to create a free-standing metallic structure, the polycarbonate membrane was etched by submerging it in dichloromethane for a few seconds, leaving the wires sitting atop the working electrode (**Fig. 1f**).

Morphology of the nanoporous membranes and the resultant nanowire networks are examined by scanning electron microscopy (SEM) using a Hitachi 4100 SEM, as shown in **Fig. 2**. The SEM images, **Fig. 2b**, clearly show the interconnecting nanowire networks, following the structure described in **Fig. 1a**. X-ray diffraction measurements (not shown) indicate that the deposited nanowires are polycrystalline, similar to earlier reports on single nanowires.[14-16]

Single sheets of the interconnected networks have densities of 100 mg/cm^3 - 500 mg/cm^3 . To form a lower density structure, a bilayer working electrode was used, comprised of Cu(50 nm)/Fe(200 nm); the thin Cu layer does not seal the pores adequately. After depositing the copper wire network the Fe electrode was chemically etched with hydrochloric acid (HCl, copper is not etched by HCl). The polycarbonate membrane with the 50 nm Cu electrode was folded onto itself and placed in dichloromethane to remove the plastic. The resulting low-density structure was held together by the thin working electrode and wire intersections ($\approx 10^9$ intersections/cm²).

To transfer the light weight structure, now suspended in dichloromethane, into air while retaining its volume, a freeze drying process was used to prevent structural collapse due to surface tension.[17,18] After the polycarbonate was etched away, the contaminated dichloromethane was gently removed and replaced by methanol. This process was performed several times until the sample is immersed in what is nearly pure methanol. A similar exchange process was performed to transfer the sample from methanol to water. The water was frozen with liquid nitrogen and the frozen sample was placed in rough vacuum (≈ 10 mTorr) to sublimate the ice away. After several hours in vacuum the sample was slowly vented to atmosphere, leaving the low-density copper structure intact and in air. Single sheets of electrode with intersecting wire lattice have a density of $\approx 125 \text{ mg/cm}^3$, which corresponds to 98.5% porosity (the ratio of air volume to total sample volume). By using the aforementioned stacking/folding/freeze-drying method, metallic nanowire

networks, consisting of multiple sheets of the free-standing structure, with density as low as 40mg/cm³ (99.5% porosity) were achieved.

Magnetization reversal in Cobalt networks

Magnetic properties of Co networks were measured on a vibrating sample magnetometer (VSM) at room temperature with applied fields up to 1.5 Tesla. The maximal field of 1.5 T is larger than the saturation for Cobalt, and thus should overcome effects such-as shape anisotropy. For comparison, both intersecting and parallel nanowire samples were investigated, which utilized Co nanowires with 75 nm diameter. Details of the magnetization reversal was further investigated using the first-order reversal curve (FORC) method.[19-26] In this measurement technique, the sample is positively saturated. Then the applied field is reduced to a reversal field, H_R , located along the descending branch of the major hysteresis loop. Then, the applied field, H , is increased from H_R to positive saturation, capturing the evolution of the magnetization, M . This process is repeated for approximately 50 values of H_R between the initial reversal events and negative saturation. Changes in the magnetic reversal behavior are isolated in the FORC distribution by applying a second-order derivative to the magnetization: $\rho(H, H_R)=d^2M/(dHdH_R)$. Recognizing that progressing to more negative H_R probes the down-switching events, and increasing H probes up-switching events, the FORC distribution can instead be presented in terms of a coercivity and bias: $H_c=(H-H_R)/2$, $H_b=(H+H_R)/2$. For this work, the data will be presented in the (H_c, H_b) coordinate space due to the natural symmetries of the FORC features in this orientation.

The parallel nanowire samples were only ion-tracked normal to the plane of the membrane, thus after etching and electrodeposition all wires were parallel to one another and perpendicular to the plane of the membrane. Magnetic hysteresis loops were measured with the field applied at an

angle θ relative to the membrane plane (for the parallel wires, $\theta=0$ and 90° corresponds to the field being perpendicular and parallel to the wires, respectively), as shown in **Fig. 3a**. Magnetometry measurements of the parallel nanowires measured at $\theta=0$ show a pinched loop with a small remanence (magnetization, M , at zero magnetic field, $H=0$). By comparison, the hysteresis loop measured at $\theta=90^\circ$ shows a much squarer structure and larger remanence. The measured hysteresis loops are consistent with the expected behavior of nanowires, in which the magnetic reversal is dominated by the shape anisotropy, which strongly encourages the moments to align along the wire.[27]

For the intersecting nanowire lattices, the ion-tracking was performed at three angles: one normal to the plane of the membrane and two at 45° from the membrane normal, at 180° azimuthal orientation; all angles were exposed to the same irradiation density. The resultant intersecting nanowire lattices are illustrated in **Fig. 2c**. Magnetometry measurements performed on the intersecting wire samples (**Fig. 3b and c**) at $\theta=90^\circ$ show a squarer loop with a large remanent magnetization, compared to measurements taken at $\theta=0$, indicating that the direction along the surface normal remains the magnetic easy axis.

Interestingly, one might expect the measurements performed with the magnetic field orthogonal to the wires (**Fig. 3a** at $\theta=0$ and **Fig. 3b** at $\phi=0$) to be the same. However, the coercivities of these loops are measured to be 270 Oe and 570 Oe, respectively, demonstrating a clear difference in the magnetic reversal behavior, even in an orientation which is dominated by the shape anisotropy.

Measuring the intersecting wire sample as the field is rotated in the plane of the intersections, **Fig. 3c**, presents an opportunity to evaluate the role of the shape anisotropy and

interwire coupling. Specifically, at $\theta = 0^\circ$, 1/3 of the wires are perpendicular to the field and 2/3 are at 45° from the applied field, at $\theta = 45^\circ$, 1/3 of the wires are perpendicular, 1/3 are parallel, and 1/3 are 45° from the applied field; at $\theta = 90^\circ$, 1/3 of the wires are parallel, and 2/3 are 45° from the applied field. As one might expect, the orientation with the largest projection along the magnetic field (e.g. $\theta = 90^\circ$) remains the magnetic easy axis. During the rotation, the shape anisotropy would typically dominate the reversal behavior of the wires, however, the intersections allow domains to traverse from wires more-aligned with the magnetic field into those less-aligned. Rotating the sample in the plane of the irradiation causes a small decrease in the remnant magnetization, but little change to the coercivity – much less than in **Fig. 3a** or **3b**

These contributions can be observed directly by using the data in **Fig. 3a** to attempt and reconstruct the data in **Fig. 3c**. For example, the an attempt to reconstruct the $\theta=0$ loop in **Fig. 3c** is made by summing 1/3 of the $\theta=0$ and 2/3 of the 45° loops in **Fig. 3a** for the parallel wires. The ‘reconstructed’ loop and measured loop are shown in red and black, respectively, in **Fig. 4**. Clearly, the reconstruction fails to model the experimental measurements. This further emphasizes the importance of the intersections to the magnetic reversal behavior and distinguishes these results in comparison to mere agglomerations of wires.

To further investigate the effects of the intersections on the magnetic properties we applied the FORC method. First, considering the isolated, parallel wires, **Fig. 5a-c**, the FORC measurements were performed by rotating the sample in the plane of the wires. Measuring the FORC distribution with the magnetic field parallel to the wire axis (e.g. the magnetic easy axis, $\theta=90^\circ$) shows a pair of elongated features oriented parallel to the H_b axis, with the feature at $H_c=0.7$ kOe indicating the hysteretic reversal, and the weaker feature at $H_c = 0$ indicating reversible behavior.[28,29] The elongation of the hysteretic feature is characteristic of demagnetizing dipolar

interactions which are strong relative to the intrinsic coercive field.[25,30,31] The feature also has a small tail along the H_c axis, which is a consequence of the intrinsic coercivity distribution resulting from grain-boundary pinning and crystallite quality, and mixed crystalline phases^{33, 34}; the coercivity distribution also causes the difference in spread in $+H_b$ and $-H_b$. The maximal spread of this feature along the $+H_b$ direction quantitatively encodes to the maximal dipole field interaction, which in this case is 1100 Oe. This feature also indicates that the nanowires reverse in isolated switching events, likely a domain nucleation then rapid expansion through the entire wire in a single step, rather than through domain nucleation and progressive growth. We note that the major feature in this plot is the hysteretic element, while the reversible feature constitutes a minor effect. Rotating the sample relative to the magnetic field does not change the shape of the FORC feature, indicating the reversal still occurs as a single switching event, but significant weight is transferred to the reversible feature. Finally, at $\theta=0^\circ$ nearly all of the FORC feature is located in the reversible feature, indicating that the magnetic moments are being forced to orient orthogonal to the nanowires and are reversibly relaxing to their preferred orientation along the nanowire due to shape anisotropy.

Next, the intersecting wires are investigated with FORC, again starting with the $\theta=90^\circ$ sample, **Fig. 5d**. While it is not immediately apparent, the FORC feature in the intersecting wires is in-fact the same as the parallel wires, representing the so-called “wishbone” feature. Specifically, the vertical feature remains readily identifiable, albeit narrower in its H_b spread, but now the tail is more pronounced. This FORC feature indicates that even in the sample comprised of intersecting wires the magnetic reversal occurs one segment at a time, rather than through domain propagation, which would generate a different FORC feature.[29] As noted above, the narrower distribution in $+H_b$, now spanning to 800 Oe, indicates a reduced interaction field – as

would be expected from the new 45° segments. The more-pronounced tail indicates that the variables that contribute to the intrinsic coercivity play a larger role here. This could mean that the sample has a larger intrinsic coercivity distribution (e.g. more defects and anisotropy distribution), but more likely is that the weaker interactions allow these details to play a larger role in the reversal. This conclusion is supported by noting that the total spread along the H_c axis is approximately equal to the intrinsic coercivity distribution plus the interaction field (which can be determined by the extent in $+H_b$). Following this analysis, the two systems possess a similar intrinsic coercivity distribution.

Rotating this sample in the plane of the wires, Fig. **5d-f**, the boomerang feature remains visible, but decreases in the H_b spread, consistent with the expected reduction in the dipolar interactions. At the largest rotation the feature collapses to be a symmetric dome centered on the H_c axis. This feature corresponds to the limit of no dipolar interactions, and the spread in H_c identifies the intrinsic coercivity distribution. This also indicates that, as the sample is rotated, the reversal mechanism persists as local, discrete events rather than domain creep. Interestingly, the comparison between the intersecting wires and the parallel wires, Fig. 5c, shows a strong effect from the wires, specifically that the distribution never collapses to only reversible behavior. This is likely due in-part to the oblique irradiation, which enforces that only 33% of the wires can be orthogonal to the field at any measurement angle, placing a limit on the reversible feature. However, we also compare the strength of the reversible feature in **Fig. 5f**, in which 67% of the wires are at 45° and 33% are at 90° relative to the field, to the corresponding isolated wires, **Fig. 5b** and **5c**, and find that the FORC results are not simply a sum of the constituent elements. We propose that the difference is illustrative of the collective magnet behavior resultant from the intersection of the wires.

A similar series of measurements were performed by rotating the sample around an axis in the plane of the wires, as shown illustratively in the insets of Fig. 5g-i. For the initial orientation, the sample is aligned with the field in the plane of the wires, and accurately reproduces the wishbone structure as reported in the analogous in-plane orientation in Fig. 5d. Rotating the sample such that the plane of the wires is 45° to the magnetic field, the wishbone structure persists, with slightly stronger reversible behavior, consistent with the increased orthogonal alignment to the wires. Rotating the sample to be 90° to the magnetic field once-more causes the majority of the FORC signal to collapse to the reversible feature, directly reproducing the parallel wire case when measured with an orthogonal field, Fig. 5c. These nearly identical FORC features (Figs. 5c and 5i) indicates that both samples are responding a nearly reversible manner to the magnetic field. Indeed, both samples have analogous alignment of the wires to the magnetic field, e.g. the field is orthogonal to the wires. In both cases, with the field orthogonal to all of the wires, the shape anisotropy dominates the magnetic orientation, resulting in the reversible behavior reported by the FORC diagrams. The continuous shift in weight between the hysteretic FORC feature and the reversible feature can be seen in Fig. 5g-i to directly follow Fig. 5a-c, again, highlighting the similar underlying mechanics, namely the shape anisotropy of the wires. However, rotating the sample in the plane of the wires shows a clear effect from the intersecting wires. Furthermore, the fact that the reversible feature remains weak at all in-plane angles further reinforces that the interconnecting wires share their magnetic reversal behavior.

In summary, nuclear track-etched membranes at multiple azimuthal angles were used as an electrodeposition template to fabricate a novel, interconnected low density metallic nanowire network. Copper networks were grown with densities as low as $40\text{mg}/\text{cm}^3$. The magnetization reversal in cobalt nanowire networks was investigated through magnetometry and the effects of

intersections on magnetization reversal were investigated by the FORC technique. Comparisons between the interconnected and isolated wires revealed similar hysteresis dominated by demagnetizing interactions when the magnetic field was applied parallel to most wires. However, rotating the interconnected wires in the plane of the intersections revealed a change to more isolated reversal behavior, but not to reversible behavior. This emphasizes the collective magnetic behavior of the interconnected wires.

References

- ¹ M. Datta and D. Landolt, *Electrochimica Acta* **45**, 2535 (2000).
- ² J. Banhart, *Prog. Mater. Sci.* **46**, 559 (2001).
- ³ L. J. Gibson, *Annu. Rev. Mater. Sci.* **30**, 191 (2000).
- ⁴ B. van Setten, M. Makkee, and J. A. Moulijn, *Catal. Rev.-Sci. Eng.* **43**, 489 (2001).
- ⁵ L. P. Lefebvre, J. Banhart, and D. C. Dunand, *Adv. Eng. Mater.* **10**, 775 (2008).
- ⁶ R. Kotz and M. Carlen, *Electrochimica Acta* **45**, 2483 (2000).
- ⁷ B. C. H. Steele and A. Heinzl, *Nature* **414**, 345 (2001).
- ⁸ P. B. Price and R. M. Walker, *Phys. Rev. Lett.* **8**, 217 (1962).
- ⁹ P. B. Price and R. M. Walker, *J. Appl. Phys.* **33**, 3407 (1962).
- ¹⁰ C. P. Bean, M. V. Doyle, and G. Entine, *J. Appl. Phys.* **41**, 1454 (1970).
- ¹¹ P. Apel, *Radiat. Meas.* **34**, 559 (2001).
- ¹² C. Schonenberger, B. M. I. vanderZande, L. G. J. Fokkink, M. Henny, C. Schmid, M. Kruger, A. Bachtold, R. Huber, H. Birk, and U. Staufer, *J. Phys. Chem. B* **101**, 5497 (1997).
- ¹³ W. T. Crawford, W. Desorbo, and J. S. Humphrey, *Nature* **220**, 1313 (1968).
- ¹⁴ K. Liu, K. Nagodawithana, P. C. Searson, and C. L. Chien, *Phys. Rev. B* **51**, 7381 (1995).
- ¹⁵ J. Wong, P. Greene, R. K. Dumas, and K. Liu, *Appl. Phys. Lett.* **94**, 032504 (2009).

- ¹⁶ J. Wong, P. Greene, R. K. Dumas, and K. Liu, Proc. SPIE **7036**, 703610 (2008).
- ¹⁷ A. Boyde and C. Wood, J. Microsc.. **90**, 221 (1969).
- ¹⁸ D. A. Gilbert, E. C. Burks, S. V. Ushakov, P. Abellan, I. Arslan, T. E. Felter, A. Navrotsky, and K. Liu, Chem. Mater. **29**, 9814 (2017).
- ¹⁹ I. D. Mayergoyz, Phys. Rev. Lett. **56**, 1518 (1986).
- ²⁰ C. R. Pike, A. P. Roberts, and K. L. Verosub, J. Appl. Phys. **85**, 6660 (1999).
- ²¹ A. P. Roberts, C. R. Pike, and K. L. Verosub, J. Geophys. Res.-Solid Earth **105**, 28461 (2000).
- ²² H. G. Katzgraber, F. Pázmándi, C. R. Pike, K. Liu, R. T. Scalettar, K. L. Verosub, and G. T. Zimányi, Phys. Rev. Lett. **89**, 257202 (2002).
- ²³ J. E. Davies, O. Hellwig, E. E. Fullerton, G. Denbeaux, J. B. Kortright, and K. Liu, Phys. Rev. B **70**, 224434 (2004).
- ²⁴ R. K. Dumas, C. P. Li, I. V. Roshchin, I. K. Schuller, and K. Liu, Phys. Rev. B **75**, 134405 (2007).
- ²⁵ D. A. Gilbert, G. T. Zimanyi, R. K. Dumas, M. Winklhofer, A. Gomez, N. Eibagi, J. L. Vicent, and K. Liu, Sci. Rep. **4**, 4204 (2014).
- ²⁶ D. A. Gilbert, B. B. Maranville, A. L. Balk, B. J. Kirby, P. Fischer, D. T. Pierce, J. Unguris, J. A. Borchers, and K. Liu, Nat. Commun. **6**, 8462 (2015).
- ²⁷ T. M. Whitney, J. S. Jiang, P. C. Searson, and C. L. Chien, Science **261**, 1316 (1993).
- ²⁸ L. C. Fanny Beron, Mariana Ciureanu, David Menard, Robert W. Cochrane and Arthur Yelon, IEEE Transactions on Magnetics **42** (2006).
- ²⁹ C. R. Pike, Phys. Rev. B **68**, 104424 (2003).
- ³⁰ X. Kou, X. Fan, R. K. Dumas, Q. Lu, Y. Zhang, H. Zhu, X. Zhang, K. Liu, and J. Q. Xiao, Adv. Mater. **23**, 1393 (2011).

³¹ C.-I. D. a. A. Stancu, Journal of Physics: Condensed Matter **25** (2012).

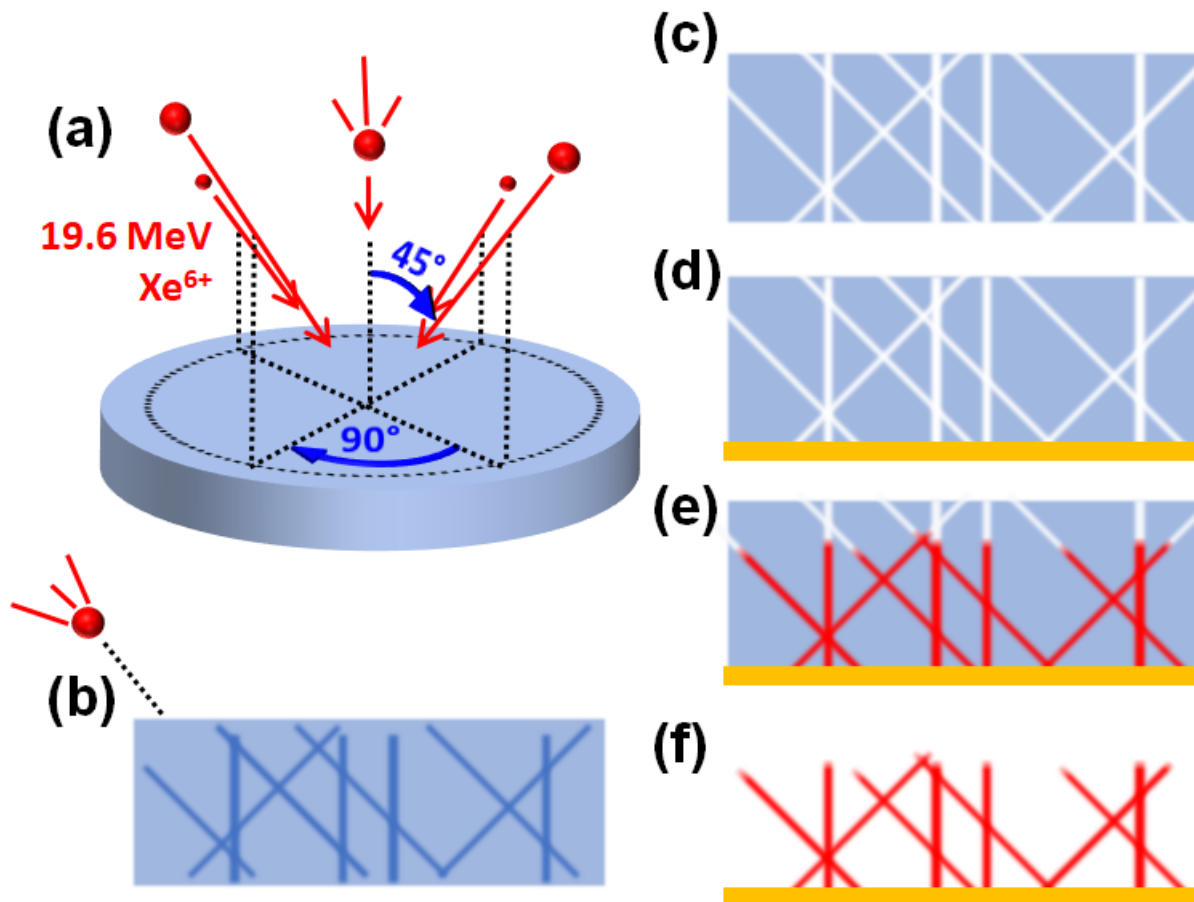


Fig. 1: Step-by-step production of the nanowire networks. Blue region represents the polycarbonate membrane. (a) Diagram of irradiation geometry, (b) cross-section of polycarbonate irradiated at multiple angles, forming damaged tracks (dark regions). (c) Etching of damaged tracks to produce interconnected nanoporous network. (d) Membrane with deposited working electrode. (e) Electrodeposition of the metal network. (f) Removal of polycarbonate membrane, leaving behind a freestanding lattice of wires atop the sputtered layer.

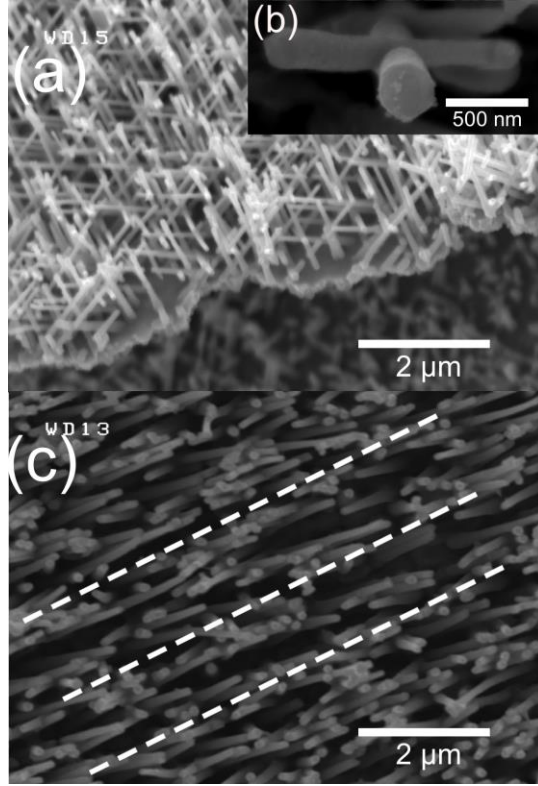


Fig. 2: (a) SEM image of an interconnected copper network on a sputtered copper working electrode. (b) Shows that at an intersection the wires are physically connected (from a different sample). (c) SEM image of a sample irradiated at three angles. This produces intersections in planes that contain the three irradiated angles (which are highlighted with white dashed lines).

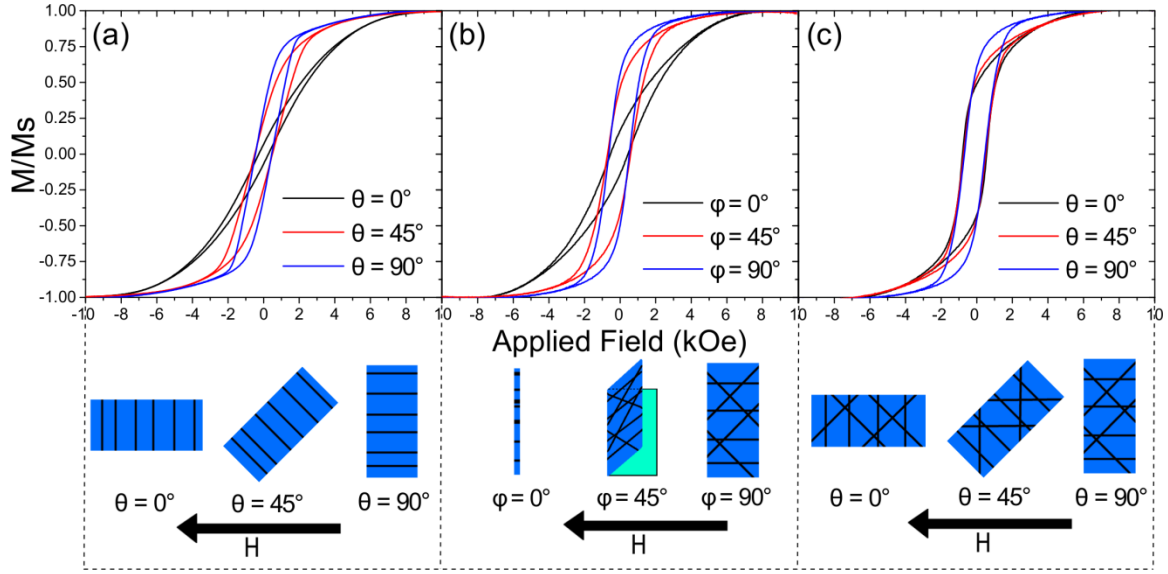


Fig. 3: Magnetic hysteresis loops measured by VSM. Below each image is a diagram illustrating the measurement geometry relative to the applied field H . The polycarbonate membrane is shown by the blue box, while the nanowires inside are shown by black lines. **(a)** Single angle irradiated sample with all wires perpendicular to, at 45° from, and parallel to the applied field (corresponding to $\theta = 0^\circ$, 45° , and 90° respectively). **(b)** Three angle irradiated sample rotated about the φ axis – the angle between the irradiation plane and the applied field H . Note from the diagrams that $\varphi = 0^\circ$ corresponds to all the wires being perpendicular to the applied field. **(c)** Three angle irradiated sample rotated about the θ axis as indicated. Here the applied field is always in the irradiation plane.

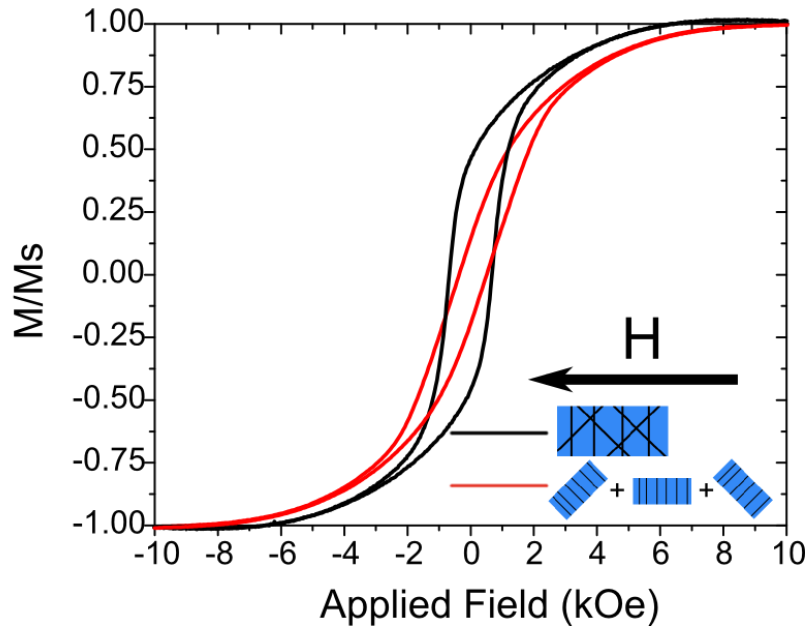


Fig. 4. The black line is a hysteresis loop for the intersecting wire sample in the geometry shown with respect to the applied field H . The red line is constructed hysteresis loop, made by adding together non-intersecting wire loops oriented at the same angles to the applied field and weighted by the number of wires at those angles to mimic the intersecting sample.

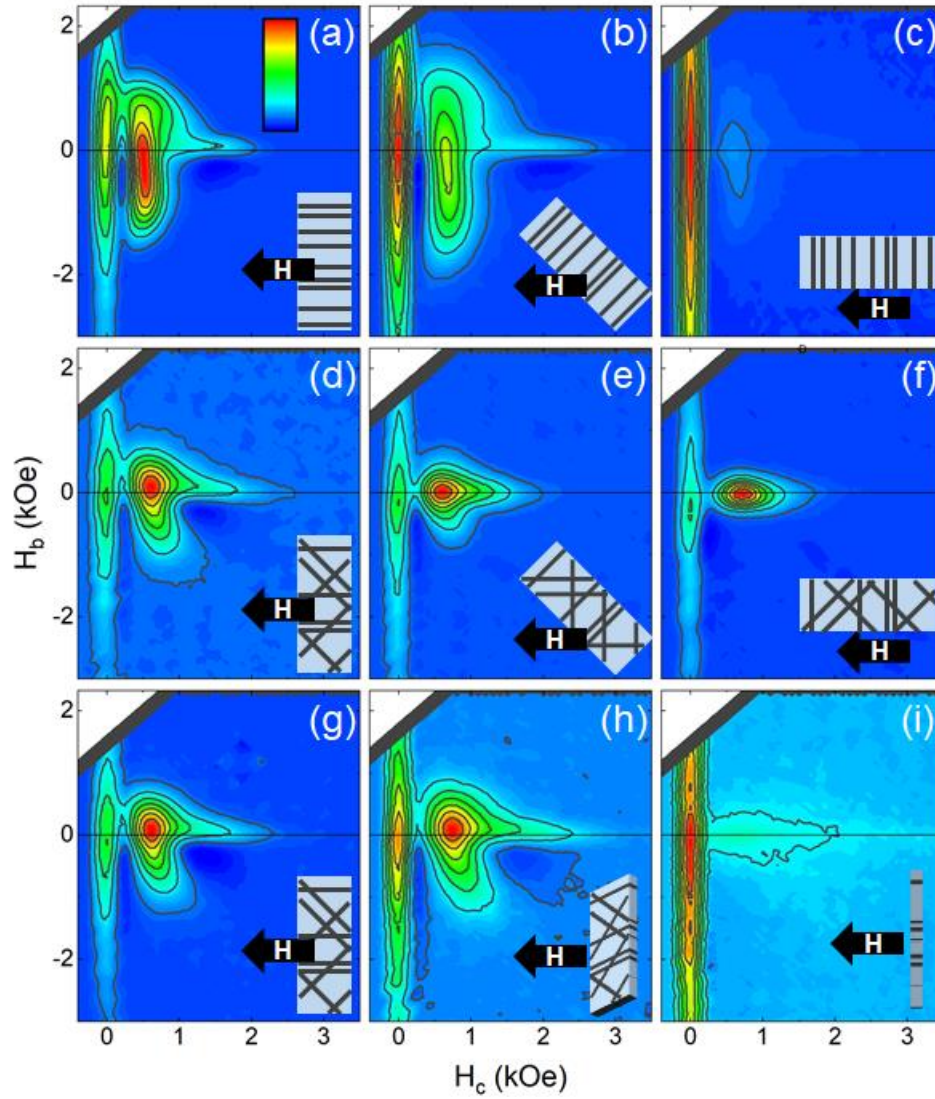


Fig. 5: FORC diagrams for (a-c) a single angle irradiated sample and (d-i) three angle irradiated sample, measured at different geometries relative to the applied field. The schematic diagrams in the lower right corner of each panel indicate the orientation of the wires (black lines) and membrane (blue box) to the applied field shown by the large black arrow. Note that due to the way measurements were conducted, *f* and *i* represent the same geometry, but measured separately.

Supplementary Materials

Given the irradiation density f of each irradiated angle, the off-normal angle θ , the thickness t of the template material, and the radius r of the resulting etched tracks the total number of intersections per unit area N can be calculated as follows. The calculation assumes the pores have the same radius along their entire lengths (a good approximation in our samples), the off-normal angle was the same and in the same plane for the two off-normal irradiations (true for our samples) and it fails to account for a wire having multiple intersections (a decent approximation). This is done by calculating the intersection density of each of the four types of intersections: N_1 , N_2 , N_3 and N_4 .

Cross sectional images of the four possible types of intersections are shown in **Fig. S1a, c, e** and **g** while **Fig. S1b, d, f** and **h** show top-down views of their respective cases. For example, **Fig. S1a** shows a cross-sectional view of a blue polycarbonate membrane with two normally irradiated pores, one in red and one in purple intersecting in a yellow region. **Fig. S1b** depicts the same case from the top, with the purple pore in an arbitrary location in the membrane and the yellow region around it showing the possible places the center of a another pore could be located to cause an intersection. This area of possible intersection multiplied by the beam irradiation density gives the average number of intersections that that particular purple pore will have with others, n_1 :

$$n_1 = f(4\pi r^2) \quad (1)$$

But this is just the intersections caused by a single pore. To calculate the intersection density caused by this first type we must multiple by the beam irradiation density again giving:

$$N_1 = 4\pi f^2 r^2 \quad (2)$$

The intersection densities for the remaining types are calculated in the same way (see the calculated areas in **Fig. S1d, f and h**):

$$N_2 = 4\pi f^2 r^2 \cos(\theta) \quad (3)$$

$$N_3 = 4\pi f^2 r^2 + 4f^2 r t \cos(\theta) \tan(\theta) \quad (4)$$

$$N_4 = 4\pi f^2 r^2 \cos(\theta) + 8f^2 r t \cos^2(\theta) \tan(\theta) \quad (5)$$

Finally, to get the total intersection density N we must add the totals from the four types and divide by two because we have counted each intersection twice using this method:

$$N = \frac{N_1 + N_2 + N_3 + N_4}{2} \quad (6)$$

For a total irradiation density of 2×10^9 tracks/cm² divided evenly across all three irradiations, pore radius of 37.5 nm, pore length of 3 μ m, $\theta = 45^\circ$, and three angles we get $N = \approx 4 \times 10^9$ intersections/cm².

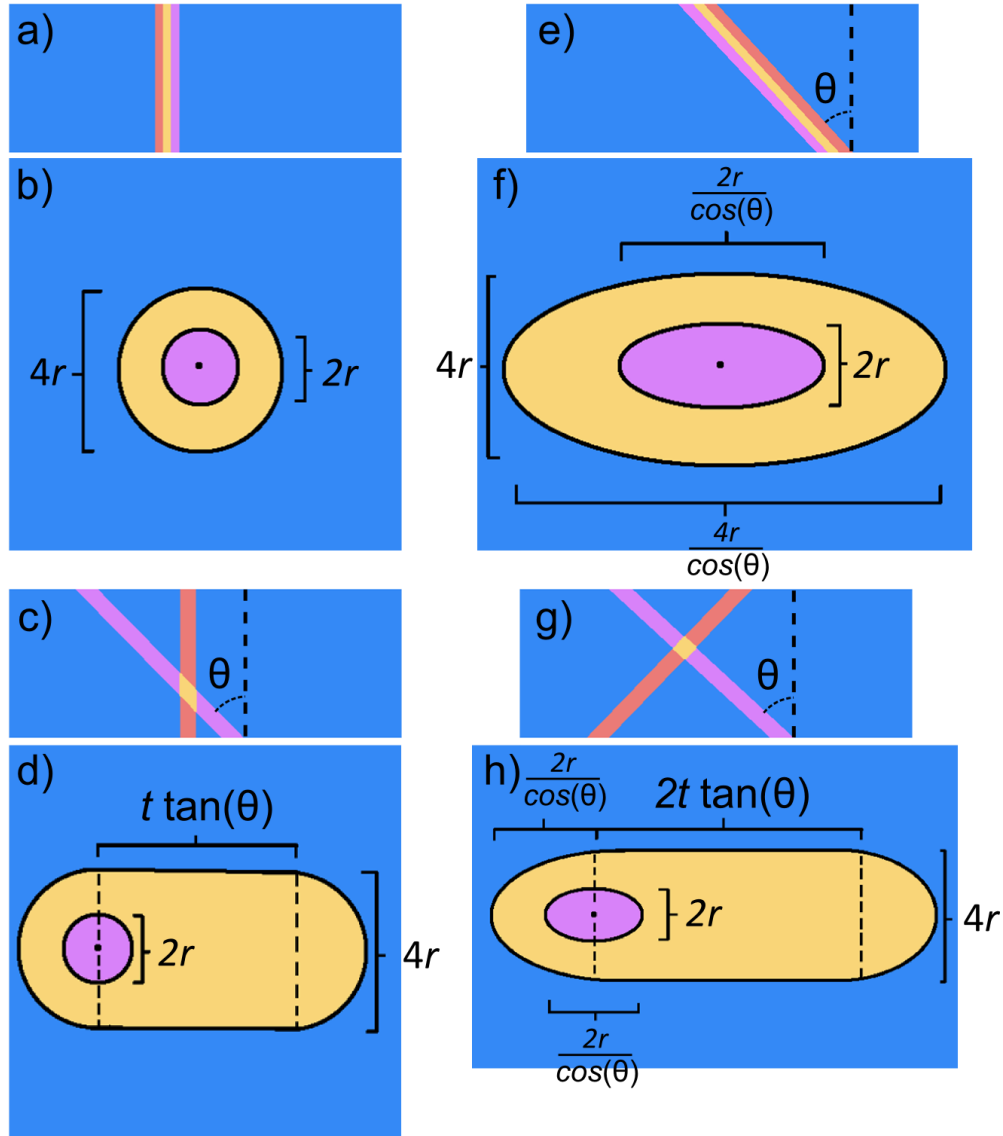


Fig. S1. Intersection probability is calculated by examining area of possible intersection in each of the four different intersection cases: two pores normal to the plane of the membrane (**a,b**), one pore normal and one at an angle θ from the plane membrane (**c,d**), two pores at an angle θ from the plane of the membrane (**e,f**) and one pore at an angle θ and the other at an angle $-\theta$ (**g,h**). In each case the first image shows a cross-section of the intersection and the second a top-down image for area calculation.